RSC Advances

PAPER

View Article Online
View Journal | View Issue

Cite this: *RSC Adv.*, 2020, **10**, 40117

Insight into the enhanced photocatalytic activity of Mo and P codoped $SrTiO_3$ from first-principles prediction

Yueqin Wang,[a] Jingyu Wang,[b] Wei Lian[b] and Yin Liu*[b]

Received 15th August 2020
Accepted 19th October 2020

DOI: 10.1039/d0ra07026b

rsc.li/rsc-advances

In this study, the synergistic effect of cation codoping (Mo and the cation P) on the band structure of $SrTiO_3$ is demonstrated to enhance its photocatalytic activity. The electronic structure and optical properties of (Mo + P) codoped $SrTiO_3$ are examined by performing GGA + *U* calculations. The results show that the strong hybridization between the Mo 4d states and the O 2p states assisted by the non-metal P leads to the formation of fully occupied and delocalized intermediate states (IBs) near the valence band of $SrTiO_3$. The proximity of IBs to the valence band resulted in the ability to separate photo-excited electrons from reaction holes, which helps to ensure efficient electron replenishment reducing the probability of trapping electrons from the CB. This kind of metal Mo and non-metal P-compensated codoping can efficiently narrow the band gap and enhance the visible-light absorption. Moreover, the positions of the band edges after codoping (Mo + P) are found to be thermodynamically favorable for water splitting.

1. Introduction

Perovskite, $SrTiO_3$, has attracted intense attention as a promising material in the fields of photocatalysis and water splitting, since it presents excellent properties such as low cost and long term stability.[1,2] Due to the large band gap of $SrTiO_3$ (3.25 eV),[3] it is, however, not able to show photocatalytic activity in the visible-light region, and can absorb only ultraviolet light (only 5% of solar energy). Besides the long term stability, an ideal photocatalyst should also have a narrow band gap to utilize cheaper visible-light, and appropriate band edge positions to meet the requirements for water splitting.[4,5] As such, there has been ever-growing interest in the band structure engineering of $SrTiO_3$. Enabling $SrTiO_3$ to absorb the more abundant visible-light is a crucial prerequisite for enhancing the photo-conversion efficiency by reducing its band gap below 2.0 eV.[6–8]

In exploring the enhanced photocatalytic activity of $SrTiO_3$-based materials to the visible-light region, there have been many reports that have adopted different strategies for optimizing the band gap and extending the light absorption of $SrTiO_3$ by different doping schemes.[9–15] Among them, the codoping approach is an effective means for lowering the band gap and improving the visible-light response, involving either cation–anion,[16–18] cation–cation,[19–21] or anion–anion[22,23] pairs. In the case of cation–cation codoping, the substitution of transition metal cations (Cr, Fe, Rh, Mo, W, *etc.*) at the host Ti sites in $SrTiO_3$ has shown to lower the band gap by introducing localized 3d impurity states, shifting the absorption spectra threshold towards the visible region.[24–27] Recently, the substitution of non-metal and metal cations at the Ti sites in TiO_2 has stimulated great interest in enhancing the visible-light absorption and photocatalytic activity by including (Fe + Si), (Mo + P) and (W + P) codoping.[28–30] However, to the best of our knowledge, there is no reported experimental or theoretical work focusing on the synergistic effects of (Mo + P) codoped $SrTiO_3$ on the band gap engineering.

The present work investigates the role of Mo and P cation codoping in $SrTiO_3$ using first-principles calculations. The substitutional positions of both the Mo and P dopants are incorporated at the Ti sites. The stabilities and optical properties of codoped systems were first determined. The electronic structure of the codoped system was analyzed and compared to gain insight into the intermediate states for lowering the band gap. To explore the synergistic effects on the redox capacity for photocatalytic water splitting, the band edge alignments were carefully carried out. These prediction results indicate that the band structure engineering of $SrTiO_3$ by codoping with metal and non-metal cations (Mo + P) is a promising strategy for enhancing photocatalytic activity.

2. Computational methods

All the spin-polarized calculations were performed using the CASTEP package in Materials Studio 8.0.[31] The exchange and correlation interaction was treated with the generalized gradient approximation (GGA) of Perdew–Burke–Ernzerhof (PBE). The interactions between the valence electrons and ionic

[a]School of Mechanics and Optoelectronic Physics, Anhui University of Science and Technology, Huainan 232001, China. E-mail: yqwang1025@126.com
[b]School of Materials Science and Engineering, Anhui University of Science and Technology, Huainan 232001, China. E-mail: yinliu@aust.edu.cn

core were approximated by the ultra-soft pseudopotentials (USPP). To reproduce the experimental band gap of 3.25 eV in $SrTiO_3$, the GGA + U_p + U_d approach was adopted to describe the correlation effects, which can predict the corrected electronic structure and optical properties.[32–34] The on-site corrections are typically applied to the d or f orbitals of transition metal oxides; however, the band gaps are still underestimated with respect to the experimental values. Theoretical studies have revealed that the corrected band electronic structures of metal oxides can be obtained by simultaneously using the on-site Coulomb corrections on the d states of transition metals and the 2p orbital of oxygen atoms. Ma *et al.* theoretically found that the simultaneous application of the on-site Coulomb corrections on the Zn-3d (U_d) and O-2p (U_p) orbitals lead to a corrected band structure of ZnO.[32] It has been also reported that the pair of U_d (10 eV) and U_p (7 eV) was identified as an optimal choice for the correct band structure of W-doped ZnO; in this work, we chose the GGA + U_d + U_p method to discuss the correction effects on the electronic structure of $SrTiO_3$ oxide materials. Based on the previous theoretical predictions, we firstly fit the U_d (2.3 eV) of Ti-3d states,[35] then discuss the effects of different U_p values on the band structures. It was found that the band gaps were 3.11, 3.22 and 3.48 eV for bulk $SrTiO_3$ system as using the U_p values (7, 8 and 9 eV) for O-2p orbitals, respectively. The correct band gap was 3.22 eV within $U_p = 8$ eV, which agrees well with the experimental results. We note that a U_p value of 8 eV is the best choice, which is somewhat larger than the U value used in previous work.[32] Taking into account the transition metal Mo dopant, we also calculated the band gap of Mo-doped $SrTiO_3$ by using Coulomb corrections on the Mo-4d. The indirect spin-down band gap is about 1.75 eV within $U_d = 4$ eV, which is very close to the band gap (1.86 eV) calculated by the HSE hybrid density functional.[36] Therefore, for a better description of the localized transition, we used the on-site repulsion $U_{eff} = 2.3$ eV and 4 eV on the Ti 3d and Mo 4d states as in previous theoretical investigations,[35,37,38] and the U of the O 2p states was set to 8 eV. Spin-polarized calculations were performed for pure and different doped $SrTiO_3$ systems. The energy cut-off for the wave function expanded in plane waves was chosen to be 400 eV, and k-point mesh with $3 \times 3 \times 3$ was used for the supercell calculation. Both the lattice parameters and the atomic positions were fully relaxed until the residual forces were smaller than 0.03 eV $Å^{-1}$, and the convergence tolerance for the optimized electronic energy was set to 1×10^{-5} eV.

To explore the optical properties, the absorption coefficients ($\alpha_{abs}(\omega)$) were simulated according to the following relation:[39]

$$\alpha_{abs}(\omega) = \sqrt{2}\omega\left[\sqrt{\varepsilon_1^2(\omega) + \varepsilon_2^2(\omega)} - \varepsilon_1(\omega)\right]^{1/2} \quad (1)$$

where ω is the angular frequency of the photon, $\varepsilon_1(\omega)$ and $\varepsilon_2(\omega)$ are the real and imaginary parts of the complex dielectric function ε, respectively. Considering the tensor nature of $\varepsilon(\omega)$ in the cubic structure, the $\varepsilon(\omega)$ are the x, y, z components in the tensor matrix. The imaginary part $\varepsilon_2(\omega)$ of the dielectric tensor is calculated using summation over the empty states, while the real part $\varepsilon_1(\omega)$ of the dielectric tensor is obtained from the Kramers–Kronig transformation, as implemented in CASTEP. Taking into account the crystal anisotropy, in the present study, the spectra along the c-axis are analyzed because the strongest absorption is along the c-axis direction.

3. Results and discussion

The presence of one electron and one hole per dopant is essential for modeling the charge compensation synergistic effect. Intense attention has been paid to B–B sites for metal–metal elements codoping (*i.e.*, Cr/Ta, Ta/Ni, and W/Cd),[40,41] which provide one electron as the donor dopant and one hole as the acceptor dopant, thus keeping the charge balance in codoping systems. The substitution of metal and non-metal dopants on the Ti sites can also introduce the charge balance. To model the Mo and P dopants codoping in $SrTiO_3$, a $2 \times 2 \times 2$ periodic supercell within 40 atoms was constructed, as shown in Fig. 1. Before investigating the electronic and optical properties of the (Mo + P) codoped $SrTiO_3$ systems, we first optimized the primitive $SrTiO_3$. The optimized lattice parameters a, b, c were 3.952 Å, consistent with previous theoretical and experimental results.[42] The GGA + U_p + U_d calculated band gap of $SrTiO_3$ was 3.22 eV, which also agrees well with the experimental (3.25 eV) and HSE calculation values (3.19 eV) due to the partial correction of the band gap by suitable U values. These results show that the parameters and computational methods (GGA + U) employed here are suitable for describing different monodoped and codoped $SrTiO_3$ systems.

The monodoped and codoped systems were constructed from the relaxed $2 \times 2 \times 2$ supercell. Considering the effect of the oxidation states of Mo and P cations on the ground states of the codoped $SrTiO_3$, we calculated the total energy of different oxidation state configurations with the pairs of (Mo^{5+}, P^{3+}), (Mo^{5+}, P^{5+}), (Mo^{6+}, P^{3+}) and (Mo^{6+}, P^{5+}) codoping. For simplicity, the energy of the (Mo^{5+}, P^{3+}) codoped configuration was set to zero, and the energies of (Mo^{5+}, P^{5+}), (Mo^{6+}, P^{3+}) and (Mo^{6+}, P^{5+}) codoped configurations were 6.7, 31.6 and 32.3 meV,

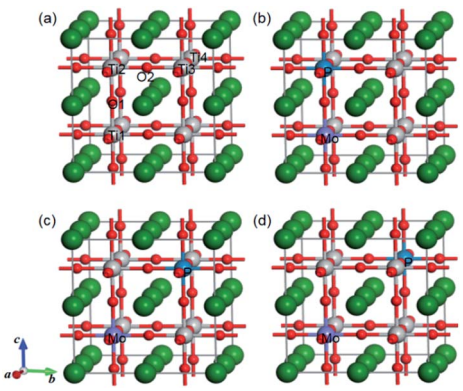

Fig. 1 The $2 \times 2 \times 2$ supercell structures of pure $SrTiO_3$ cubic crystal (a), the (Mo + P) codoped $SrTiO_3$ with the near configuration (b), the medium configuration (c), and the far configuration (d). The dark green, gray and red balls represent the Sr, Ti and O atoms, respectively. The Mo and P dopants are marked in violet and blue, respectively.

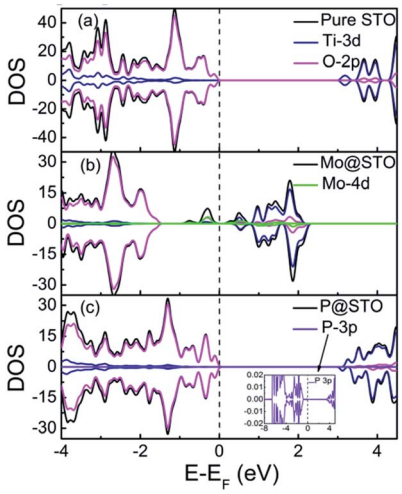

Fig. 2 TDOS and PDOS of (a) pure $SrTiO_3$, (b) Mo monodoped $SrTiO_3$, and (c) P monodoping. The Fermi level is set at zero energy.

respectively. It is noted that the (Mo^{5+}, P^{3+}) codoped configuration possesses the lowest total energy, which is considered to be the ground state. We used one Mo^{5+} cation to substitute for a Ti^{4+} host site to produce an electron per supercell, while one P^{3+} cation substituted for a Ti^{4+} site to introduce a hole per supercell. For the Mo or P-monodoped $SrTiO_3$ system, there was only one doping configuration due to the symmetry of the cubic crystal, thus the Mo or P was substituted at the Ti1 site as labeled in Fig. 1(a). According to the relative substitute positions of Mo and P dopants, there are three different configurations for the (Mo + P) codoping. For the convenience of discussion, the three configurations are defined as the "near", "medium" and "far" configurations, respectively, as shown in Fig. 1(b)–(d). For the near configuration, the Mo and P dopants occupy the nearest neighboring Ti sites at Ti1 and Ti2 sites, respectively. While for the medium and far configurations, the (Mo, P) dopant pairs substitute at (Ti1, Ti3) and (Ti1, Ti4), respectively. For the cases of three (Mo + P) codoped $SrTiO_3$ systems, the near configuration was found to be energetically more stable by 0.07 and 0.22 eV than the medium and the far configurations, respectively. Although the nearest neighbour codoping configuration was found to be more energetically attainable in experimental techniques such as hydrothermal and sol–gel methods,[43,44] the dopants will enter the lattice sites randomly in the supersonic cluster beam deposition techniques.[45] Therefore, to provide a theoretical basis for the design and fabrication of new photocatalysts, in the following sections, we discuss the electronic structure and optical properties of all three codoped configurations.

To obtain detailed insight into the doping effect of the Mo/P on the electronic structure of $SrTiO_3$, we first calculated the total DOS and partial DOS (PDOS) of pure and monodoped models, as shown in Fig. 2. For the pure $SrTiO_3$, the valence band maximum (VBM) and conduction band minimum (CBM) were mainly contributed by the O 2p states and Ti 3d states, respectively, as shown in Fig. 2(a). The Mo monodoped $SrTiO_3$ was modeled by introducing one Mo dopant at the host Ti1 site. The highest occupied orbital energy level was shifted to near the CBM after Mo doping, which is ascribed to the downward shift of the VBM and CBM. Here, the Fermi level was set at zero energy (CASTEP takes the energy of the highest occupied orbitals as the energy zero by default). That is to say, the Mo-doped $SrTiO_3$ system shows a typical n-type semiconductor nature due to the electron doping. The CBM was significantly downward shifted to lower energy, and some mid-gap impurity states appeared as isolated states within the forbidden gap, which can greatly narrow the band gap of $SrTiO_3$, as shown in Fig. 2(b). Analysis of PDOS showed that these localized impurity states originated from the strong hybridization of the Mo 4d and O 2p states. The lower energy of the Mo 4d orbital than the Ti 3d orbital induced the spin-up partially occupied states 0.74 eV above the VB and unoccupied states 0.23 eV below the CB, which can be interpreted by the different valence electron configurations of Mo ($5s^24d^4$) and Ti ($4s^23d^2$). Substitution of a Ti^{4+} site with a Mo^{5+} dopant leads to the intrinsic donor defects in $SrTiO_3$, which typically acts as trapping centers for charge carriers to depress the photocatalytic activity. In the case of P cation doping, there was no variation in the VBM but a slight upward shifting of the CBM, as shown in Fig. 2(c), which displays p-type doping character. In this case, the band gap expands slightly to 3.34 eV. Some spin states lying above the CBM do not originate from the P 3p impurity orbitals but from the Ti 3d states due to lattice distortion. Due to the large differences in ionic radius between the dopant P (0.44 Å) and the host Ti (0.605 Å) elements, the perturbation in the lattice structure is relatively large. Based on these results, we considered the charge compensation effects of the Mo and P codoping on $SrTiO_3$ to solve the above problems, and then enhance the photocatalytic performance.

To evaluate the relative difficulty for the incorporation of dopants into the host lattice in experiments, we calculated the formation energies (E_f) of different (Mo + P) codoping configurations. The smaller the formation energy, the easier the substitutional doping is;[46] that is to say, the stability of the doped $SrTiO_3$ with different substitutional sites is determined by the relative formation energy. The formation energies of monodoped Mo and P, and the codoped (Mo + P) $SrTiO_3$ systems are defined as follows:

$$E_f = E_{monodoped} - E_{pure} + \mu_{Ti} - \mu_{Mo/P} \quad (2)$$

and

$$E_f = E_{codoped} - E_{pure} + 2\mu_{Ti} - \mu_{Mo} - \mu_P \quad (3)$$

where the E_{pure}, $E_{monodoped}$ and $E_{codoped}$ are the total energy of pure $SrTiO_3$, Mo or P monodoped, and (Mo + P) codoped $SrTiO_3$ systems, respectively. μ_{Ti}, μ_{Mo} and μ_P denote the chemical potentials of Ti, Mo and P atoms, respectively; the formation energies can vary as a function of the oxygen chemical potential for doped systems.[47] In this study, we also considered the effect of the oxygen environment (either O-rich or Ti-rich growth conditions) on the formation energy. At the equilibrium

Table 1 Calculated defect formation energies of Mo/P monodoped and codoped $SrTiO_3$ in the O-rich and Ti-rich conditions, which are denoted as E_f^{O-rich} and $E_f^{Ti-rich}$ (eV), respectively. The defect pair binding energies (E_b, in eV) of the three (Mo + P) codoped $SrTiO_3$ configurations are also listed

Dopants	$E_f^{O\text{-}rich}$ (eV)	$E_f^{Ti\text{-}rich}$ (eV)	E_b (eV)
Mo	−8.987	3.599	—
P	−15.349	−2.762	—
(Mo + P)-near	−24.768	0.405	0.433
(Mo + P)-medium	−24.696	0.478	0.359
(Mo + P)-far	−24.549	0.625	0.213

conditions between the $SrTiO_3$ and the reservoirs of Sr, Ti and O elements, the following relation must be satisfied:

$$\mu_{Sr} + \mu_{Ti} + 3\mu_O = \mu_{SrTiO3} \quad (4)$$

where μ_{Sr}, μ_{Ti} and μ_O are the chemical potentials of Sr, Ti, O elements. In the present study, the μ_{Sr} and μ_{Ti} were calculated from the energy per atom in the respective bulk crystals. Under O-rich growth conditions, μ_O was simulated from the energy of one O atom in the O_2 molecule placed at the centre of a 15 × 15 × 15 Å^3 cubic box, and the μ_{Ti} was determined by formula (4). Under Ti-rich conditions, μ_{Ti} amounts to the energy of one Ti atom in bulk Ti and the μ_O is assumed by the formula (4). The calculated formation energies of doped $SrTiO_3$ systems are listed in Table 1. For Mo monodoping, the E_f values were −8.987 and 3.599 eV under O-rich and Ti-rich conditions, respectively, implying that for the monodoping of Mo in $SrTiO_3$, it is difficult for Mo to enter into the lattice under Ti-rich conditions in experiments. In contrast, for P cation monodoping, the predicted E_f under O-rich and Ti-rich conditions are −15.349 and −2.762 eV, respectively, which indicates that the substitution of one Ti^{4+} by a P^{3+} cation can be more easily realized under O-rich conditions than that under Ti-rich conditions. Compared with the monodoping, we found that the E_f decreases after codoping. In the cases of three (Mo + P) codoped configurations, E_f is negative for all of them under O-rich conditions, suggesting that the synthesis of (Mo + P) codoped $SrTiO_3$ is feasible in an O-rich environment. However, for (Mo + P) codoping under the Ti-rich conditions, the synthesis may be rather difficult due to the positive E_f values.

To examine the coupling strength between the Mo–P dopant pairs in the codoped models, we calculated the defect pair binding energy (E_b), according to the following equation:

$$E_b = E_{Mo} + E_P - E_{Mo+P} - E_{pure} \quad (5)$$

where E_{Mo}, E_P, E_{Mo+P}, and E_{pure} represent the total energies of the Mo monodoped $SrTiO_3$, the P monodoped $SrTiO_3$, the (Mo + P) codoped $SrTiO_3$, and the pure $SrTiO_3$, respectively, calculated using the same supercell. The calculated binding energies of the three (Mo + P) codoped configurations are also summarized in Table 1. A positive E_b implies that the defect pair is stable with respect to the isolated defect. For three codoped configurations, E_b was predicted to be 0.433, 0.359 and 0.213 eV, respectively,

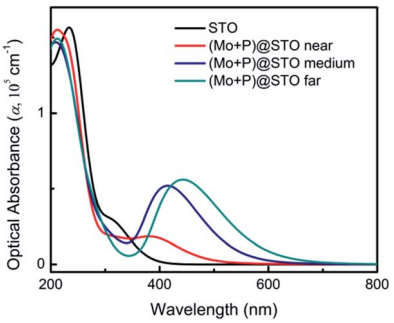

Fig. 3 Optical absorption spectra for the pure and (Mo + P) codoped $SrTiO_3$.

indicating that donor–acceptor Mo–P pairs are more stable as compared to the corresponding isolated impurities in $SrTiO_3$, which may be attributed to the electron transfer from the P to Mo impurity. We found that the E_b value decreased with the increase in the distance from the defect pairs, which is ascribed to the reduced charge transfer from non-metal P to metal Mo.

The optical absorption of the codoped $SrTiO_3$ is strongly related to its photocatalytic activity. Here, we calculated the optical absorption coefficients of three codoped $SrTiO_3$ systems and compared them with the results of pure $SrTiO_3$; the results are shown in Fig. 3. The calculated optical absorption spectra of pure $SrTiO_3$ is consistent with previous experimental and theoretical results.[48,49] The pure $SrTiO_3$ can only respond to UV light, which has no absorption activity in the visible-light region. The gradient curves with their absorption edges all extend into the visible-light region for three (Mo + P) codoped $SrTiO_3$ configurations, and a new optical absorption peak was observed in the wavelength range of 365–650 nm. In comparison, the medium configuration and the far configuration had even higher absorption efficiencies than that in the near case, due to narrower band gaps. The maximum absorption edges can be

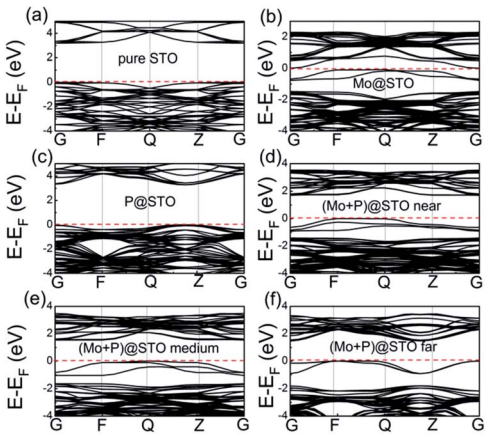

Fig. 4 Band structure of $SrTiO_3$ before and after doping: (a) pure $SrTiO_3$, (b) Mo-doped $SrTiO_3$, (c) P-doped $SrTiO_3$, (d) (Mo + P) codoped $SrTiO_3$ within near configuration, (e) (Mo + P) codoped $SrTiO_3$ within medium configuration, and (f) (Mo + P) codoped $SrTiO_3$ within far configuration.

extended to 649 nm for the far configuration. The (Mo + P) codoped $SrTiO_3$ system showed significantly improved absorption performance, which indicates its potential for application as a visible-light-driven photocatalyst. These prominent visible absorptions from our predicted calculations are comparable to previous works on $SrTiO_3$ with different codoping.[50]

In general, the optical properties of codoped $SrTiO_3$ are mainly determined by their electronic band structures.[51] As shown in Fig. 4, we first calculated the band structure of monodoped Mo/P, codoped (Mo + P) $SrTiO_3$ systems, and compared them with that of pure $SrTiO_3$. For the Mo monodoped case, there are several spin-up partially occupied impurity bands just below the CB, as shown in Fig. 4(b), which can be ascribed to the presence of one more electron in the shell of the Mo dopant ($5s^24d^3$) than that in the host Ti ($4s^23d^2$). Since donor states are localized near to the CBM, we assumed that the band gap was calculated as the direct gap between the impurity states and the VBM of about 0.74 eV. Attractive candidates for photocatalytic water splitting must have a suitable band gap ranging from 1.5 to 3.0 eV, although the Mo monodoped $SrTiO_3$ can efficiently narrow the band gap; note that a relatively smaller band gap is not suitable for water splitting. For the P monodoped case, one P^{3+} cation is substituted at the host Ti^{4+} of perovskite $SrTiO_3$, which will introduce one hole into the system. From Fig. 4(c), we see that the bandwidth of the P monodoped $SrTiO_3$ is even higher than that of pure $SrTiO_3$, which is also not suitable for water splitting. In view of the band structure engineering, the formation of the charge non-compensation defects and the partially occupied impurity bands in Mo or P monodoped $SrTiO_3$ can facilitate the formation of recombination centers, which will decrease the photocatalytic performance.

To overcome these problems, we studied the effect of (Mo + P) compensated codoping on the band gap of $SrTiO_3$. The obtained energy band structures of (Mo + P) codoped $SrTiO_3$ configurations are plotted and shown in Fig. 4. For the near configuration, there is a spin-up intermediate bands (IBs) with a width of 0.86 eV, which is located below the Fermi level, as shown in Fig. 4(d). The intrinsic forbidden gap is divided into two sub-gaps by the presence of such IBs. In this case, the host band gap decreased significantly to 1.73 eV. Compared with the narrow band gap of about 0.74 eV in Mo monodoped $SrTiO_3$, the (Mo + P) codoped system exhibited an indirect band gap with an ideal value. On the one hand, the IBs can be stepping stones to improving the excitation of electrons to the CB under low photon energy, which will promote the absorption efficiency. On the other hand, the IBs can also act as a trapping center, which will promote the electron and hole recombination. However, the excitation or recombination depends on the energy difference between the VB and IBs or CB and IBs. Usually, the shallow impurity states near the VB are beneficial for the charge separation; in contrast, the deep impurity states near the CB can easily become recombination centers. As seen from Fig. 5, the energy difference between the VBM and the IBs minimum is much smaller than that between the CBM and the IBs maximum. This means that the probability for a VB hole to pump up into the IBs will be greater than the probability for a CB electron to combine with a hole in the IBs;[52] *i.e.*, the IBs can facilitate electron excitation and enhance the photocatalytic efficiency. We also noted that the IBs that appeared below the Fermi level in (Mo + P) codoped system are fully occupied states. By the introduction of Mo and P dopants, these fully filled IBs near the VBM can lead to photo-excitation from the IBs to the CB directly, reducing the chance of electron–hole recombination. Here, we also find that the partially occupied bands of Mo monodoped $SrTiO_3$ preferred to be located near the CBM, which can act as a carrier-trapping center. For the (Mo + P) codoped cases, the fully occupied IBs were moved to the nearby VBM due to the synergistic effect of charge compensation codoping. As shown in Fig. 4(e) and (f), for the medium and far configurations cases, there are also some fully occupied IBs below the energy zero level. Moreover, the CBMs of both configurations showed slight downward shifts as compared with the near configuration, which further narrowed the band gap.

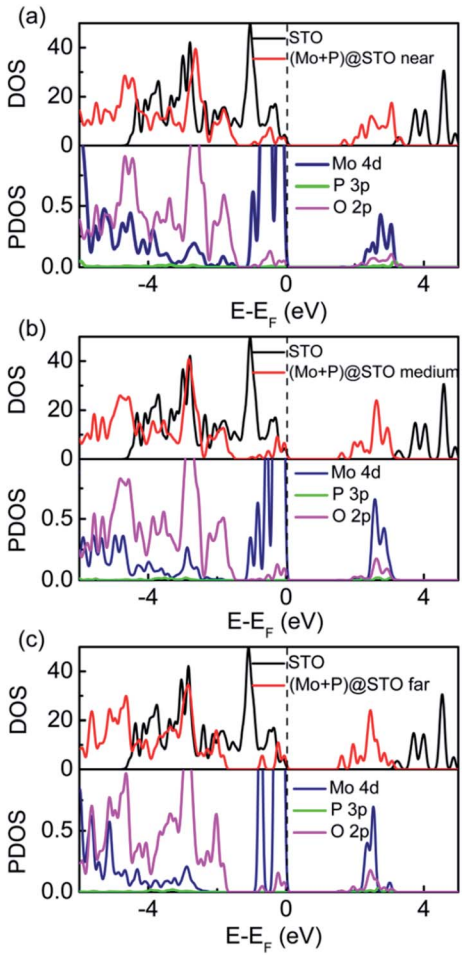

Fig. 5 TDOS and the corresponding PDOS of Ti 3d, O 2p, Mo 4d and P 3p electrons. (a) (Mo + P) codoped $SrTiO_3$ within near configuration, (b) (Mo + P) codoped $SrTiO_3$ within medium configuration, and (c) (Mo + P) codoped $SrTiO_3$ within far configuration. The Fermi level is set at zero energy.

To further understand the origin of the enhanced optical performance of $SrTiO_3$, we calculated the total DOS and partial DOS of (Mo + P) codoped $SrTiO_3$ and compared them with that of pure $SrTiO_3$, as shown in Fig. 5. For three (Mo + P) codoped

$SrTiO_3$ configuration cases, all of the VBMs and CBMs positions shifted towards the low-energy direction, inducing narrowed band gaps of 1.73, 1.59 and 1.49 eV, respectively. These narrowed band gaps are greatly helpful for exciting electrons from the VB to the CB and broadening the optical absorption spectra edge. As seen from Fig. 5, there are IBs located near the VBs in the three codoping cases, and they appeared as non-continuous states above the VBM, which is located below the Fermi level, suggesting that the IBs are fully occupied. The partial DOS results imply that the IBs mainly originated from the hybridization of Mo 4d and O 2p states, as shown in the bottom panel of Fig. 5(a)–(c). The impurity Mo 4d states appeared far below the CBMs due to the more negative energy of the Mo 4d orbital than the Ti 3d orbital. However, for the three codoping cases, the presence of the partially occupied Mo 4d states in the CB can facilitate the formation of the CB with Mo 4d character, which is different from the Ti 3d character in the pure $SrTiO_3$. Interestingly, within the band gap of the CBs, there is slight hybridization from the P 3p and O 2p states, indicating weak P–O coupling in the (Mo + P) codoped $SrTiO_3$, which also leads to the CBM shifting to the low-energy direction. For the (Mo + P) codoped $SrTiO_3$ system, the delocalized and fully occupied IBs formed by the p–d coupling can effectively narrow the band gap and induce the band downward shift to about 1.9 eV as compared with that of the pure $SrTiO_3$. These can lead to a decrease in the photo-excitation energy; thus the absorption edge is extended to the visible light region due to the synergistic effect of the Mo and P codoping. In particular, some photogenerated electrons were excited directly from the IBs to the CB in the presence of both Mo and P dopants, which could be responsible for the fact that the new absorption peaks (365–650 nm) appeared in the above optical spectra (see Fig. 3).

To describe the hybridization in the (Mo + P) codoped $SrTiO_3$, we plotted the charge density distribution in the (010) planes for pure $SrTiO_3$, codoped within the near and the medium configurations and in (011) planes for the far configuration, as shown in Fig. 6. The distances between the neighbouring elements on the same surface were obtained from CASTEP outcome files, while the distances between other elements were graphically measured linear distances. For comparison, the charge density of the pure $SrTiO_3$ is plotted in Fig. 6(a). It was found that the Ti–O bonds were in the form of covalent bonds in pure $SrTiO_3$. Checking the inner part of the optimized geometry of the pure $SrTiO_3$, the labeled atom positions correspond to that in Fig. 1(a), the Ti1–Ti2, Ti1–Ti3, and Ti1–Ti4 distances were 3.922, 5.546, and 6.793 Å, respectively and the Ti1–O1 bond length was 1.961 Å. For the three (Mo + P) codoped systems, the Mo atom substituted for the Ti1 atom, and the P atom replaced the Ti2, Ti3 and Ti4 atoms in the three cases, respectively. The optimized Mo–P distances in the three cases were 3.899, 5.512, 6.755 Å, respectively, showing obvious contractions as compared with those corresponding to the Ti–Ti distances in pure $SrTiO_3$. Moreover, the Mo–O bonds in the three codoped models were 2.207, 2.017 and 2.007 Å, respectively, which are larger than that of the Ti1–O1 bond (1.961 Å) before codoping, indicating that the covalency of the Mo–O bond is weaker than that of Ti–O bond. In contrast, due to the relatively small atomic radius of the P atom, the entered P dopant generated a large lattice distortion. This could be because the P–O bond lengths in the three codoped cases were 1.682, 1.715 and 1.734 Å, respectively, which are significantly smaller as compared to those of the Ti1–O1 bonds in pure $SrTiO_3$. Such the relatively shortened P–O bond lengths indicate that the P dopant is strongly bonded to the nearest O atom. As shown in Fig. 6(b)–(d), after (Mo + P) codoping, the Mo–O bond showed the typical covalent nature, and there was charge transfer from the nearest neighboring O atoms to the Mo dopants. Moreover, the P–O bonds in the three codoped configurations displayed a significant degree of covalency. We observed that the charge density around the P dopant was lower than that of the near O atoms, which is mainly due to the relatively large electronegativity of the O atom.

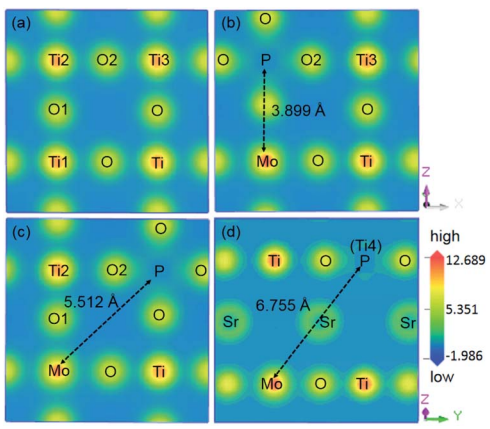

Fig. 6 Charge density distribution in the (010) plane for (a) pure $SrTiO_3$, (b) the near codoped configuration, and (c) the medium codoped configuration. Charge density distribution in the (011) plane for (d) the far codoped configuration.

It is well known that the photoconversion efficiency of a semiconductor for water splitting to produce hydrogen is governed by the position of the band edge with respect to the redox potential. Theoretically, the relevant potential level of donor dopants is required to be more negative than the valence band potential, while the potential level of acceptor species needs to be more positive than the conduction band potential. In order to describe the oxidation and reduction capacity of the (Mo + P) codoped $SrTiO_3$ systems, the CBM (E_{CB}) and VBM (E_{VB}) are calculated empirically according to the following formula:

$$E_{CB} = X - \frac{1}{2}E_g - E_0 \quad (6)$$

where E_g is the band gap, X is the absolute electronegativity of the perovskite oxide catalyst, and E_0 is the energy of free electrons on the hydrogen scale (~4.5 eV). The valence band tops (E_{VB}) were calculated from the respective band gaps.

To estimate the water reduction performance of different (Mo + P) codoped systems, the band alignments with respect to the water redox levels of three different codoped $SrTiO_3$ systems as well as pure $SrTiO_3$ were calculated and plotted on one diagram, as shown in Fig. 7. For the pure $SrTiO_3$ system, the

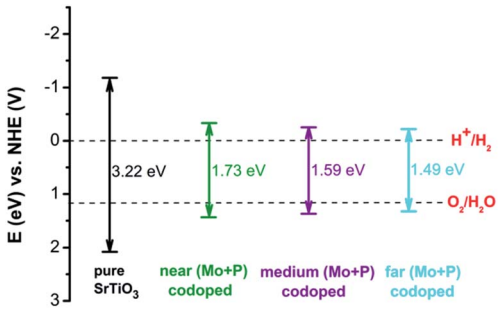

Fig. 7 The band edge alignment of the pure and codoped $SrTiO_3$ systems with respect to the water redox band edge position potentials.

Table 2 Calculated CBM (eV) and VBM (eV) potentials *vs.* NHE for the pure and (Mo + P) codoped cases

Model	$SrTiO_3$	(Mo + P)-near	(Mo + P)-medium	(Mo + P)-far
E_{CB} (eV)	−1.17	−0.34	−0.27	−0.22
E_{VB} (eV)	2.05	1.39	1.32	1.27

calculated band gap is 3.22 eV, in which the VBM is located 1.17 eV below the water oxidation (H_2O/O_2) level and the CBM lies 0.82 eV above the water reduction (H^+/H_2) level, and this is consistent with the experimental results.[53] For three (Mo + P) codoped $SrTiO_3$ configurations, there were IBs in the forbidden band with band widths of 0.86, 1.05 and 0.95 eV, respectively. These fully occupied IBs can be considered as stepping-stones to bridging the VBM and the CBM, thus photo-generated electrons are directly excited from the IBs to the CB. As seen from Fig. 7, the (Mo + P) codoping can effectively narrow the band gap by introducing the delocalized energy levels, and also greatly perturb the positions of both the VBM and CBM. As for the three (Mo + P) codoped $SrTiO_3$ configurations, the band edge positions of both the VBM and CBM straddle the water redox potential levels, which meet the thermodynamic criterion for hydrogen production in solar-light-driven water splitting.

The calculated CBM and VBM potentials *vs.* NHE for the different systems are listed in Table 2. The calculated E_{CB} and E_{VB} of pure $SrTiO_3$ are −1.17 and 2.05 eV, respectively, which possesses a strong reducing ability under UV light due to its more negative CBM than the water reduction potential (0 eV *vs.* NHE at pH 0). Moreover, its VBM is more positive than the water oxidation potential level (1.23 eV *vs.* NHE). Therefore, it has the capacity for photocatalytic water splitting. As mentioned previously in the literature, the enhanced oxidation or reduction capacity depends on the downward shift of the VBM or the upward shift of the CBM, respectively.[54,55] In the cases of the three (Mo + P) codoped configurations, the CBMs shifted upward by 0.83, 0.90 and 0.95 eV, respectively, as compared to the pure $SrTiO_3$, which implies that the photo-reduction ability is enhanced, and the absorption edges move towards the visible light region. The VBMs of the three codoped systems moved downward as compared to that of pure $SrTiO_3$ by 0.66, 0.73 and 0.78 eV, respectively, which means that the oxidation ability is also improved. From the calculated E_{CB} and E_{VB} in Table 2, we can deduce that splitting water into H_2 with the (Mo + P) codoped $SrTiO_3$ photocatalyst is thermodynamically feasible. The results show that the (Mo + P) codoped $SrTiO_3$ system possessed the more suitable band gap and band edge positions for photocatalytic water splitting.

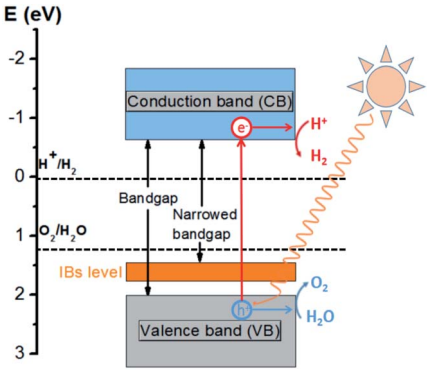

Fig. 8 Schematic plot of the energy band alignment of the (Mo + P) codoped $SrTiO_3$ Photocatalyst and the redox potential of the water-splitting reaction.

Solar energy provides an attractive way to produce hydrogen *via* water splitting. When the energy of the incident light is larger than the band gap of the $SrTiO_3$-based catalytic materials, electrons and holes are generated in the VB and CB, respectively. The photo-generated electrons (e^-) and holes (h^+) that migrate from the bulk of the semiconductor towards the reaction sites on the photocatalyst surface without recombination can reduce and oxidize water molecules to produce hydrogen and oxygen, respectively. A schematic diagram of the (Mo + P) codoped $SrTiO_3$ photocatalyst for water splitting is shown in Fig. 8. Based on the above electronic band structure, the introduction of Mo and P dopants in metal oxide will generate new IBs energy levels between the VBM and CBM, resulting in the narrowed minimum light absorption energy gap of the host lattice. This will reduce the photon excitation energy from the VB to CB, thus extending its range of optical absorption to the visible-light region. Furthermore, the proximity of IBs to the VB allows for efficient electron replenishment, which possesses ability to separate photoexcited electrons from reaction holes, reducing the probability of trapping electrons from the CB, so the photocatalytic activity of the (Mo + P) codoped $SrTiO_3$ system will be good. As schematically depicted in Fig. 8, the band edge potential of the (Mo + P) codoped $SrTiO_3$ photocatalyst by theoretical prediction is appropriate for water-oxidation/-reduction processes.

4. Conclusion

We have explored the metal/non-metal (Mo + P) codoping effects on the electronic structure and photocatalytic performance of $SrTiO_3$ based on first principles predictions. Theoretical results indicate that the (Mo + P) codoped $SrTiO_3$ is feasible in O-rich environments due to low formation energy. The (Mo + P) codoping leads to a strong hybridization between

Mo 4d and O 2p, which induces the fully occupied and delocalized IBs near the valence band, possessing the ability to separate photo-excited electrons from reaction holes and reducing the probability of trapping electrons from the CB. We found that both the strong Mo–O hybridization and weak P–O coupling can narrow the band gap of $SrTiO_3$, and also improve its photocatalytic performance. The calculated optical absorption spectra of the (Mo + P) codoped $SrTiO_3$ also verified the improved visible light absorption by donor–acceptor pair codoping. The band edge positions of the (Mo + P) codoped $SrTiO_3$ system also satisfy the criterion for water splitting.

Conflicts of interest

There are no conflicts to declare.

Acknowledgements

This work is supported by the Key Projects of Natural Science Foundation of Colleges and Universities of Anhui Province (KJ2019A0117), Stand-up Fund for Talent Introduction of Anhui University of Science and Technology, the College Physics Teaching Team of Anhui Province (2019jxtd046), the Top Talents of Colleges and Universities of Anhui Province (GxbjZD14), and the Key Technologies R&D Program of Anhui Province of China (1604a0802122 and 17030901091).

References

1 S. Patial, V. Hasija, P. Raizada, P. Singh, A. A. Parwaz, A. Singh and A. M. Asiri, Tunable photocatalytic activity of $SrTiO_3$ for water splitting: strategies and future scenario, *J. Environ. Chem. Eng.*, 2020, **8**, 103791.

2 B. L. Phoon, C. W. Lai, J. C. Juan, P. L. Show and G. T. Pan, Recent developments of strontium titanate for photocatalytic water splitting application, *Int. J. Hydrogen Energy*, 2019, **44**, 14316–14340.

3 K. V. Benthem, C. Elsässer and R. H. French, Bulk electronic structure of $SrTiO_3$: experiment and theory, *J. Appl. Phys.*, 2001, **90**, 6156–6164.

4 K. V. Sopiha, O. I. Malyi, C. Persson and P. Wu, Band gap modulation of $SrTiO_3$ upon CO_2 adsorption, *Phys. Chem. Chem. Phys.*, 2017, **19**, 16629–16637.

5 K. Sivula and R. van de Korol, Semiconducting materials for photoelectrochemical energy conversion, *Nat. Rev. Mater.*, 2016, **70**, 16010.

6 M. Rioult, H. Magnan, D. Stanescu and A. Barbier, Single crystalline hematite films for solar water splitting: Ti-doping and thickness effects, *J. Phys. Chem. C*, 2014, **118**, 3007–3014.

7 Y. Yang, W. J. Zheng, D. J. Cheng and D. P. Cao, Designing transition metal and nitrogen-codoped $SrTiO_3$ (001) perovskite surfaces as efficient photocatalysts for water splitting, *Sustainable Energy Fuels*, 2017, **1**, 1968–1980.

8 H. Muhammad, L. Xu, L. Zhou, Z. P. Zheng, Q. Y. Fu and W. Luo, Exceptional co-catalyst free photocatalytic activities of B and Fe co-doped $SrTiO_3$ for CO_2 conversion and H_2 evolution, *Nano Res.*, 2018, **11**, 6931–6404.

9 H. Yu, J. Wang, S. Yan, T. Yu and Z. G. Zou, Elements doping to expand the light response of $SrTiO_3$, *J. Photochem. Photobiol., A*, 2014, **275**, 65–71.

10 F. P. Cai, Y. B. Tang, F. Y. Chen, Y. Yan and W. D. Shi, Enhanced visible-light-driven photocatalytic degradation of tetracycline by Cr doping $SrTiO_3$ cubic nanoparticles, *RSC Adv.*, 2015, **5**, 21290–21296.

11 B. Modak and S. K. Ghosh, Insight into the enhanced photocatalytic activity of $SrTiO_3$ in the presence of a (Ni, V/Nb/Ta/Sb) pair, *Phys. Chem. Chem. Phys.*, 2018, **20**, 20078–20087.

12 L. Ye, X. Hu, X. Wang, F. L. Chen, D. Tang, D. H. Dong and K. Xie, Enhanced CO_2 electrolysis with a $SrTiO_3$ cathode through a dual doping strategy, *J. Mater. Chem. A*, 2019, **7**, 2764–2772.

13 C. Zhang, Y. Z. Jia, Y. Jing and Y. Yao, New insights into assessing the favorable codoping dopants with various co-doped cases for the band gap engineering of $SrTiO_3$, *Int. J. Hydrogen Energy*, 2015, **40**, 1343–1351.

14 H. W. Kang, S. N. Lim and S. B. Park, Co-doping schemes to enhance H_2 evolution under visible light irradiation over $SrTiO_3$: Ni/M (M = La or Ta) prepared by spray pyrolysis, *Int. J. Hydrogen Energy*, 2012, **37**, 5540–5549.

15 H. W. Kang and S. B. Park, Improved performance of tri-doped photocatalyst $SrTiO_3$: Rh/Ta/F for H_2 evolution under visible light irradiation, *Int. J. Hydrogen Energy*, 2016, **41**, 13970–13978.

16 Y. Y. Liu, W. Zhou, C. Wang, L. L. Zhou and P. Wu, Electronic structure and optical properties of $SrTiO_3$ codoped by W/Mo on different cationic sites with C/N from hybrid functional calculations, *Comput. Mater. Sci.*, 2018, **146**, 150–157.

17 W. J. Shi, *Ab initio* study on band-gap narrowing in $SrTiO_3$ with Nb–C–Nb codoping, *Phys. Rev. B: Condens. Matter Mater. Phys.*, 2011, **84**, 1541–1545.

18 Y. Liu, W. Zhou and P. Wu, Electronic structure and optical properties of Ta-doped and (Ta, N)-codoped $SrTiO_3$ from hybrid functional calculations, *J. Appl. Phys.*, 2017, **121**, 075102.

19 B. Modak and S. K. Ghosh, Origin of enhanced visible light driven water splitting by (Rh, Sb)-$SrTiO_3$, *Phys. Chem. Chem. Phys.*, 2015, **17**, 15274–15283.

20 T. S. Jamil, H. A. Abbas, A. M. Youssief, E. S. Mansor and F. F. Hammad, The synthesis of nano-sized undoped, Bi doped and Bi, Cu co-doped $SrTiO_3$ using two sol-gel methods to enhance the photocatalytic performance for the degradation of dibutyl phthalate under visible light, *Cron. Chim.*, 2017, **20**, 97–106.

21 W. Chen, H. Liu, X. Y. Li, S. Liu, L. Gao, L. Q. Mao, Z. Y. Fan, W. F. Shangguan, W. J. Fang and Y. S. Liu, Polymerizable complex synthesis of $SrTiO_3$:(Cr/Ta) photocatalysts to improve photocatalytic water splitting activity under visible light, *Appl. Catal., B*, 2016, **192**, 145–151.

22 J. L. Yan and Y. N. Zhao, DFT study on electronic structure and optical properties of N-doped, S-doped, and N/S co-doped $SrTiO_3$, *Phys. B*, 2012, **55**, 654–659.

23 H. F. Liu, Effect of nitrogen and carbon doping on electronic properties of $SrTiO_3$, *Solid State Commun.*, 2012, **152**, 2063–2065.

24 P. Reunchan, N. Umezawa, S. Ouyang and J. H. Ye, Mechanism of photocatalytic activities in Cr-doped $SrTiO_3$ under visible-light irradiation: an insight from hybrid density-functional calculations, *Phys. Chem. Chem. Phys.*, 2012, **14**, 1876–1880.

25 A. Yamakata, M. Kawaguchi, R. Murachi, M. Okawa and I. Kamiya, Dynamics of photogenerated charge carriers on Ni- and Ta-doped $SrTiO_3$ photocatalysts studied by time-resolved absorption and emission spectroscopy, *J. Phys. Chem. C*, 2016, **120**, 7997–8004.

26 Y. Yamaguchi, S. Usuki, K. Yamatoya, N. Suzuki, K. Katsumata, C. Terashima, A. Fujishima, A. Kudo and K. Nakata, Efficient photocatalytic degradation of gaseous acetaldehyde over ground Rh–Sb co-doped $SrTiO_3$ under visible light irradiation, *RSC Adv.*, 2018, **8**, 5331–5337.

27 M. M. Fadlallah, M. F. Shibl, T. J. H. Vlugt and U. Schwingenschlögl, Theoretical study on cation codoped $SrTiO_3$ photocatalysts for water splitting, *J. Mater. Chem. A*, 2018, **6**, 24342–24349.

28 W. Du, Q. Xu, D. Q. Jin, Y. Shu, L. M. Kong and X. Y. Hu, Visible-light-induced photo-fenton process for the facile degradation of metronidazole by Fe/Si codoped TiO_2, *RSC Adv.*, 2018, **8**, 40022–40034.

29 Y. M. Lin, Z. Y. Jiang, C. Y. Zhu, X. Y. Hu, H. Y. Zhu, X. D. Zhang, J. Fan and S. H. Lin, The optical absorption and hydrogen production by water splitting of (Si,Fe)-codoped anatase TiO_2 photocatalyst, *Int. J. Hydrogen Energy*, 2013, **38**, 5209–5214.

30 A. EI Mragui, O. Zegaoui, I. Daou and J. Silva, Preparation, characterization, and photocatalytic activity under UV and visible light of Co, Mn, and Ni mono-doped and (P,Mo) and (P,W) co-doped TiO_2 nanoparticles: a comparative study, *Environ. Sci. Pollut. Res.*, 2019, DOI: 10.1007/s11356-019-04754-6.

31 S. J. Clark, M. D. Segall, C. J. Pickard, P. J. Hasnip, M. I. J. Probert, K. Refson and M. C. Payne, First principles methods using CASTEP, *Z. Kristallogr.*, 2005, **220**, 567–570.

32 X. Ma, Y. Wu, Y. H. Lv and Y. F. Zhu, Correlation effects on lattice relaxation and electronic structure of ZnO within the GGA + U formalism, *J. Phys. Chem. C*, 2013, **117**, 26029–26039.

33 J. P. Li, H. T. Lu, Y. H. Li, S. H. Meng and Y. M. Zhang, First-principles generalized gradient approximation (GGA) + U_d + U_p studies of electronic structures and optical properties in cubic HfO_2, *Solid State Commun.*, 2015, **211**, 38–42.

34 M. Nolan and G. W. Watson, Hole localization in Al doped silica: A DFT + U description, *J. Chem. Phys.*, 2006, **125**, 144701.

35 Z. P. Hu and H. Metiu, Choice of U for DFT + U Calculations for Titanium Oxides, *J. Phys. Chem. C*, 2011, **115**, 5841–5845.

36 B. Modak, K. Srinivasu and S. K. Ghosh, A hybrid DFT based investigation of the photocatalytic activity of cation–anion codoped $SrTiO_3$ for water splitting under visible light, *Phys. Chem. Chem. Phys.*, 2014, **16**, 24527–24535.

37 Y. Q. Wang, C. Zhang, Y. Liu, M. X. Zhang and F. F. Min, Efficient visible-light-induced photocatalytic activity of $SrTiO_3$ co-doped with Os and N: A GGA + U investigation, *Phys. Status Solidi B*, 2019, **256**, 1800574.

38 H. Lee, M. Y. Jeong, J. H. Sim, H. Yoon, S. Ryee and M. J. Han, Charge density functional plus U calculation of lacunar spinel GaM_4Se_8 (M = Nb, Mo, Ta, and W), *Europhys. Lett.*, 2019, **15**, 47005.

39 J. Wang, Q. Meng, J. Huang, Q. Li and J. L. Yang, Band structure engineering of anatase TiO_2 by metal-assisted P–O coupling, *J. Chem. Phys.*, 2014, **140**, 174705.

40 J. W. Shi, S. H. Shen, Y. B. Chen, L. J. Guo and S. S. Mao, Visible light-driven photocatalysis of doped $SrTiO_3$ tubular structure, *Opt. Express*, 2012, **20**, A351–A359.

41 R. Niishiro, H. Kato and A. Kudo, Nickel and either tantalum or niobium-codoped TiO_2 and $SrTiO_3$ photocatalysts with visible-light response for H_2 or O_2 evolution from aqueous solutions, *Phys. Chem. Chem. Phys.*, 2005, **7**, 2241–2245.

42 W. Chang, J. A. Bellotti, S. W. Kirchoefer and J. M. Pond, Strain tensor effects on $SrTiO_3$ incipient ferroelectric phase transition, *J. Electroceram.*, 2005, **77**, 173–187.

43 V. Jeyalakshmi, R. Mahalakshmy, K. R. Krishnamurthy and B. Viswanathan, Strontium titanates with perovskite structure as photo catalysts for reduction of CO_2 by water: influence of co-doping with N, S & Fe, *Catal. Today*, 2018, **300**, 152–159.

44 L. G. Devi and B. G. Anitha, Effective band gap engineering by the incorporation of Ce, N and S dopant ions into the $SrTiO_3$ lattice: exploration of photocatalytic activity under UV/solar light, *J. Sol-Gel Sci. Technol.*, 2020, **94**, 50–66.

45 M. Chiodi, C. P. Cheney, P. Vilmercati, E. Cavaliere, N. Mannella, H. H. Weitering and L. Gavioli, Enhanced dopant solubility and visible-light absorption in Cr–N codoped TiO_2 nanoclusters, *J. Phys. Chem. C*, 2012, **116**, 311–318.

46 Q. Hou, C. Zhao and Z. Xu, Effect of Zr doping on the electrical and optical properties of ZnO, *Chem. Phys. Lett.*, 2016, **658**, 336–342.

47 Y. Liu, W. Zhou and P. Wu, Tuning electronic structure and optical properties of $SrTiO_3$ by site-specific doping by Nb with N/B from hybrid functional calculations, *Mater. Chem. Phys.*, 2017, **195**, 170–175.

48 T. Ohno, T. Tsubota, Y. Nakamura and K. Sayama, Preparation of S, C cation-codoped $SrTiO_3$ and its photocatalytic activity under visible light, *Appl. Catal., A*, 2005, **288**, 74–79.

49 V. Mishra, A. Sati, M. K. Warshi, A. B. Phatangare, S. Dhole, V. N. Bhoraskar, H. Ghosh, A. Sagdeo, V. Mishra, R. Kumar and P. R. Sagdeo, Effect of electron irradiation on the optical properties of $SrTiO_3$: an experimental and theoretical investigations, *Mater. Res. Express*, 2018, **5**, 036210.

50 B. Modak and S. K. Ghosh, Exploring the role of La codoping beyond charge compensation for enhanced hydrogen evolution by Rh–$SrTiO_3$, *J. Phys. Chem. B*, 2015, **119**, 11089–11098.

51 R. Ahuja, O. Eriksson and B. Johansson, Electronic and optical properties of $BaTiO_3$ and $SrTiO_3$, *J. Appl. Phys.*, 2001, **90**, 1854.

52 J. H. Liu, M. Y. Weng, S. B. Li, X. Chen, J. H. Cen, J. S. Jie, W. J. Xiao, J. X. Zheng and F. Pan, High throughput HSE study on the doping effect in anatase TiO_2, *Phys. Chem. Chem. Phys.*, 2020, **22**, 39–53.

53 Y. Schoonen and A. A. Martin, The absolute energy positions of conduction and valence bands of selected semiconducting minerals, *Am. Mineral.*, 2000, **85**, 543–556.

54 L. Xu, Z. L. Ma, Q. Li, T. Chen, B. J. Peng, J. Zeng, Y. B. Zhang, K. W. Luo, L. L. Wang and C. J. Shuai, 2D layered SiC/C_2N van der Walls type-II heterostructure: a visible-light-driven photocatalyst for water splitting, *New J. Chem.*, 2020, **36**, 15439–15445.

55 S. C. Han, Y. Li and Z. Wang, $PtSe_2$/SiH van der Walls type-II heterostructure: a high efficiency photocatalyst for water splitting, *Phys. Chem. Chem. Phys.*, 2020, **30**, 17145–17151.

